Weighted Procrustes Analysis for Diffusion Tensor Imaging

Diwei Zhou, Ian L. Dryden, Alexey A. Koloydenko, and Li Bai

Abstract—**There has been substantial interest in the development of methods for processing diffusion tensor fields, taking into account the non-Euclidean nature of the tensor space. In this paper, we generalise Procrustes analysis to weighted Procrustes analysis for diffusion tensor smoothing, interpolation, regularisation and segmentation in which an arbitrary number of tensors can be processed efficiently with the additional flexibility of controlling their individual contributions. An algorithm has been developed for calculating the weighted Procrustes mean tensor. A weighted regularisation model with Procrustes size-and shape metric is proposed which incorporates the smoothness of the neighbourhood and the regularisation with the diffusion behaviour of interest. Our methods and a study of Procrustes anisotropy measure are illustrated on both synthetic and real diffusion tensor data.**

Index Terms—**Diffusion tensor, Procrustes analysis, Regularisation, Smoothing, Interpolation, Anisotropy measure.**

I. Introduction

Diffusion tensor imaging (DTI) is an advanced magnetic resonance imaging (MRI) modality which provides a unique insight into tissue structure and organisation *in vivo*. In DTI, the probability density function of a water molecule displacement over a fixed time in a voxel is that of a zero-mean multivariate Gaussian distribution [1] and its covariance matrix is proportional to the diffusion tensor. Many methods have been proposed to estimate the diffusion tensor, such as least squares methods [2],[3] and Bayesian frameworks [4],[5]. Once the diffusion tensor is estimated, its eigensystem can be calculated which plays a significant role in DTI. The eigenvectors and eigenvalues of the diffusion tensor coincide with the main diffusion directions and associated diffusivities in the tissue [6]. In particular, the principal eigenvector corresponding to the largest eigenvalue represents the mean fibre orientation at each voxel. The anisotropy of water diffusion can be captured quantitatively using tensor-derived diffusion anisotropy measures [7], such as Mean Diffusivity (MD), Fractional Anisotropy (FA), Relative Anisotropy (RA) and Geodesic Anisotropy (GA) [8]. DTI has been applied to the study of diseases such as multiple sclerosis, schizophrenia, and stroke [9]. White matter tractography [10] is another promising application of DTI for investigating brain connectivity. However, the estimation of diffusion tensors is noise-sensitive due to artifacts and limitations resulting from DTI measurements [11].

There has been substantial interest in the development of approaches for diffusion tensor processing. A regularisation scheme was proposed to process the tensor field using diffusion direction maps and diffusion anisotropy maps [12]. A k-means algorithm with the Mahalanobis distance has been proposed for clustering the tensors in the thalamus [13]. The Euclidean metric was used in level set segmentation methods [14], [15] for grouping tensor data of particular interest. However, the usual Euclidean method is often unsatisfactory for diffusion tensors due to the non-Euclidean nature of the diffusion tensor. One defect with Euclidean calculus is that non-positive semi-definite symmetric matrices can appear during Euclidean computation, e.g. in extrapolation [16]. To overcome this problem, several non-Euclidean approaches were developed. Recently, the affine-invariant Riemannian [8],[17], [18] and log-Euclidean [16] metrics using the matrix logarithm have been proposed for diffusion tensor smoothing and interpolation. Procrustes analysis is another promising non-Euclidean approach to diffusion tensor processing [19],[20]. In particular, the full shape Procrustes and Procrustes size-and-shape metrics are invariant under simultaneous rotation and reflection of the tensors. The full Procrustes shape metric is also invariant under individual scaling of the tensors, and the Procrustes metrics can deal with some rank-deficient tensors unlike the Riemannian and log-Euclidean metrics [19].

This paper focuses on generalising Procrustes analysis to weighted Procrustes analysis for diffusion tensor processing including smoothing, interpolation, regularisation and segmentation in which an arbitrary number of tensors can be processed efficiently with the additional flexibility of controlling their individual contributions. In Section II, some non-Euclidean metrics including the log-Euclidean, Riemannian, power Euclidean, full ordinary Procrustes and Procrustes size-and-shape metrics are reviewed. A weighted Procrustes averaging method and the corresponding numerical algorithm are proposed for diffusion tensor smoothing and interpolation in Section

D. Zhou is with the School of Technology, University of Wolverhampton, Wolverhampton, WV1 1LY, UK. Email: D.Zhou@wlv.ac.uk.

I. L. Dryden is with the Department of Statistics, University of South Carolina, Columbia, SC 29208, USA. Email: dryden@mailbox.sc.edu.

A. A. Koloydenko is with the Mathematics Department, Royal Holloway, University of London, Egham, Surrey, TW20 0EX, UK. Email: Alexey.Koloydenko@rhul.ac.uk.

L. Bai is with the School of Computer Science, University of Nottingham, Jubilee Campus, Nottingham NG8 1BB, UK. Email: bai@cs.nott.ac.uk.

III. Then in Section IV we develop a weighted regularisation model which incorporates the smoothness of the neighbourhood and regularisation with a diffusion behaviour of the user's choice, which can be exercised locally. The Procrustes size-and shape metric is of our main interest in this weighted regularisation model with applications for tensor field regularisation and segmentation. Results of anisotropy studies and diffusion tensor processing will be illustrated on both synthetic and real DT-MR data in Section V.

II. Background

A. Logarithm-based metrics

Let $\Omega(3)$ be the space of real symmetric 3×3 matrices and $\Omega_+(3)$ be the space of the 3×3 positive definite symmetric matrices. Then the diffusion tensor $\mathbf{D} \in \Omega_+(3)$. The Riemannian and log-Euclidean metrics are based on the tensor logarithm. The affine-invariant Riemannian metric between two diffusion tensors $\mathbf{D}_1$ and $\mathbf{D}_2$ is given by [8], [17], [18]

$$d_R(\mathbf{D}_1, \mathbf{D}_2) = \| \log(\mathbf{D}_1^{-1/2}\mathbf{D}_2\mathbf{D}_1^{-1/2}) \|, \quad (1)$$

where $\| \mathbf{A} \| = \sqrt{\text{trace}\{\mathbf{A}^T\mathbf{A}\}}$ is the Euclidean norm (also known as the Frobenius norm). A gradient descent algorithm for obtaining the mean diffusion tensor estimates of more than two tensors based on this metric was proposed in [17]. The log-Euclidean metric which is similar to the above Riemannian metric but with simpler calculation is given by [16]

$$d_L(\mathbf{D}_1, \mathbf{D}_2) = \| \log(\mathbf{D}_1) - \log(\mathbf{D}_2) \| . \quad (2)$$

Note that metrics (1) and (2) require the tensors to be strictly positive definite, whereas the space can be relaxed to positive semi-definite symmetric matrices for the metrics below in (3), (5), (6).

B. Power Euclidean metric

The power Euclidean metric is another possible metric given by [19]

$$d_A(\mathbf{D}_1, \mathbf{D}_2) = \frac{1}{|\alpha|} \| \mathbf{D}_1^\alpha - \mathbf{D}_2^\alpha \|, \quad (3)$$

where $\mathbf{D}^\alpha = \mathbf{E}\mathbf{\Lambda}^\alpha\mathbf{E}^T$, and $\mathbf{E}$ and $\mathbf{\Lambda}$ are such that $\mathbf{D} = \mathbf{E}\mathbf{\Lambda}\mathbf{E}^T$, and the power α is nonzero and real. Note that the Euclidean ($\alpha = 1$), and root Euclidean ($\alpha = 1/2$), and log-Euclidean ($\alpha \to 0$) are all special cases of the power Euclidean metric.

C. Ordinary Procrustes Analysis

Procrustes analysis is a powerful shape analysis tool for matching configurations as closely as possible using the similarity transformations (rotation, translation and scaling) [21], [22]. To ensure the symmetric positive semi-definiteness of $\mathbf{D}$, a new reparameterisation

$$\mathbf{D} = \mathbf{Q}\mathbf{Q}^T \quad (4)$$

was suggested [5] where $\mathbf{Q}$ is a general 3×3 matrix. Then, $\mathbf{D}_1 = \mathbf{Q}_1\mathbf{Q}_1^T$ and $\mathbf{D}_2 = \mathbf{Q}_2\mathbf{Q}_2^T$. A Procrustes size-and-shape metric was introduced to match $\mathbf{Q}_1$ (from $\mathbf{D}_1$) and $\mathbf{Q}_2$ (from $\mathbf{D}_2$) under rotation, reflection and translation while often preserving scale information. The Procrustes size-and-shape metric is given by [19]

$$d_S(\mathbf{D}_1, \mathbf{D}_2) = \| \mathbf{Q}_1 - \mathbf{Q}_2\hat{\mathbf{R}} - \mathbf{1}_3\hat{\boldsymbol{\gamma}}^T \| \quad (5)$$

where $\mathbf{R} \in O(3)$ is a 3×3 rotation and reflection matrix and $O(3)$ is the space of 3×3 orthogonal matrices. A 3×1 location vector is denoted by $\boldsymbol{\gamma}$. Note $\mathbf{1}_3$ is the 3×1 vector of ones. The solution $(\hat{\mathbf{R}}, \hat{\boldsymbol{\gamma}})$ has been given in [19].

The full ordinary Procrustes metric between $\mathbf{D}_1$ and $\mathbf{D}_2$ using rotation, translation and scaling is defined by [19]

$$d_F(\mathbf{D}_1, \mathbf{D}_2) = \left\| \frac{\mathbf{Q}_1}{\|\mathbf{Q}_1\|} - \hat{\beta}\mathbf{Q}_2\hat{\mathbf{R}} - \mathbf{1}_3\hat{\boldsymbol{\gamma}}^T \right\| \quad (6)$$

where ($\hat{\mathbf{R}}$, $\hat{\beta}$, $\hat{\boldsymbol{\gamma}}$) is the solution to the minimisation of a squared Euclidean distance given by

$$S_F(\mathbf{D}_1, \mathbf{D}_2) = \| \mathbf{Q}_1 - \beta\mathbf{Q}_2\mathbf{R} - \mathbf{1}_3\boldsymbol{\gamma}^T \|^2 . \quad (7)$$

where $\beta > 0$ is a scale parameter. The solution ($\hat{\mathbf{R}}$, $\hat{\beta}$, $\hat{\boldsymbol{\gamma}}$) has been explicitly described [22], [23]. Note that d_F is invariant under individual scalings of $\mathbf{D}_1$, $\mathbf{D}_2$, i.e.

$$d_F(\beta_1\mathbf{D}_1, \beta_2\mathbf{D}_2) = d_F(\mathbf{D}_1, \mathbf{D}_2) \quad (8)$$

for $\beta_1 > 0$ and $\beta_2 > 0$.

D. Anisotropy

Fractional anisotropy (FA) is one of the most popular diffusion anisotropy measures in the MRI community. FA gives an estimate of the proportion of the 'magnitude' of $\mathbf{D}$ that can be ascribed to anisotropic diffusion [24]. The definition of FA is given by

$$FA = \frac{\sqrt{3[(\lambda_1 - \bar{\lambda})^2 + (\lambda_2 - \bar{\lambda})^2 + (\lambda_3 - \bar{\lambda})^2]}}{\sqrt{2(\lambda_1^2 + \lambda_2^2 + \lambda_3^2)}}, \quad (9)$$

where $\bar{\lambda} = \sum_{i=1}^{3} \lambda_i/3$. FA ranges from 0 for complete isotropy to 1 for linear anisotropy. For example, when $\lambda_1 \gg \lambda_2 = \lambda_3$, FA$\approx 1$. When $\lambda_1 = \lambda_2 \gg \lambda_3$, FA$\approx 1/\sqrt{2}$. FA maps are therefore intuitive to interpret when the white matter is rendered white and grey matter - dark.

A new anisotropy measure, Procrustes anisotropy (PA), has been proposed based on the full ordinary Procrustes metric (6) [19]. The definition of PA is given by

$$\begin{aligned} PA(\mathbf{D}) &= \sqrt{\frac{3}{2}} d_F(\mathbf{I}_{3\times 3}, \mathbf{D}) \\ &= \sqrt{\frac{3}{2} \sum_{i=1}^{3} (\sqrt{\lambda_i} - \overline{\sqrt{\lambda}})^2 / \sum_{i=1}^{3} \lambda_i} \end{aligned} \quad (10)$$

where $\overline{\sqrt{\lambda}} = \sum_{i=1}^{3} \sqrt{\lambda_i}/3$. It is clear that PA is a normalisation of the full ordinary Procrustes distance

from any given diffusion tensor $\mathbf{D}$ to the identity tensor, representing the case of ideal isotropy. As in the case of FA, the range of PA is $[0,1]$ with 0 and 1 corresponding to extreme isotropy and anisotropy, respectively.

An anisotropy measure based on the power Euclidean metric with power α is a generalisation of FA given by

$$FA(\mathbf{D}^\alpha) = \left\{ \frac{3}{2} \sum_{i=1}^{3} (\lambda_i^\alpha - \overline{\lambda^\alpha})^2 / \sum_{i=1}^{3} \lambda_i^{2\alpha} \right\}^{1/2}, \qquad (11)$$

where $\overline{\lambda^\alpha} = \sum_{i=1}^{3} \lambda_i^\alpha / 3$. It is noted that FA and PA of $\mathbf{D}$ are both members of $FA(\mathbf{D}^\alpha)$ when $\alpha = 1$ and $\alpha = 1/2$ respectively. Since $FA(\mathbf{D}^\alpha)$ is an increasing function of α (see APPENDIX for proof), $PA(\mathbf{D}) \leq FA(\mathbf{D})$, i.e. PA maps may generally appear darker than FA maps in the same region. At the same time, in some regions of high diffusion anisotropy PA provides better contrast than FA. A comparison of PA and FA is discussed in Section V-B.

III. Weighted Procrustes Averaging

We present here the non-Euclidean method of weighted Procrustes averaging for defining a sample mean of N ($N \geq 2$) diffusion tensors. The contribution of a diffusion tensor to the mean tensor is quantified by the corresponding weight which provides an additional flexibility of controlling each tensor in the group.

A. Weighted Fréchet mean

Consider a sample of N diffusion tensors $\mathbf{D}_1$,..., $\mathbf{D}_N$ where $\mathbf{D}_i \in \Omega_+(3)$, $i = 1, \ldots, N$. We assume that the $\mathbf{D}_i$ are independent and identically distributed (i.i.d.) from a distribution with mean $\mathbf{T}$ although care must be taken in defining what is a mean in a non-Euclidean space. The sample weighted Fréchet mean is defined by [25], [16]

$$\hat{\mathbf{T}} = \arg\inf_{\mathbf{T}} \sum_{i=1}^{N} w_i d^2(\mathbf{D}_i, \mathbf{T}) \qquad (12)$$

where d is a metric and the weights w_i satisfy $w_i \geq 0$ and $\sum_{i=1}^{N} w_i = 1$, and in applications can be, for example, a decreasing function of the Euclidean distance from the location of interest to the sampling locations (e.g., voxels).

B. Weighted Procrustes mean

A weighted Procrustes framework is proposed to estimate the Fréchet mean tensor $\hat{\mathbf{T}}$ when $d = d_S$ is the Procrustes size-and-shape metric, defined in (5). The weighted Procrustes mean is given by

$$\hat{\mathbf{T}}_W = \arg\inf_{\mathbf{T}} \sum_{i=1}^{N} w_i d_S^2(\mathbf{D}_i, \mathbf{T}). \qquad (13)$$

Specifically,

$$\hat{\mathbf{T}}_W = \hat{\mathbf{Q}}_W \hat{\mathbf{Q}}_W^T, \qquad (14)$$

where $\hat{\mathbf{Q}}_W = \sum_{i=1}^{N} w_i \mathbf{Q}_i \hat{\mathbf{R}}_i$ and the orthogonal matrices $\hat{\mathbf{R}}_i$, $i = 1, \ldots, N$ minimise S_W, the sum of weighted squared Euclidean distances, which is given by

$$S_W(\mathbf{D}_1, ..., \mathbf{D}_N) = \sum_{i=1}^{N} w_i \parallel \mathbf{Q}_i \mathbf{R}_i - \sum_{j=1}^{n} w_j \mathbf{Q}_j \mathbf{R}_j \parallel^2 \qquad (15)$$

and $\mathbf{Q}_i$ is the decomposition matrix of $\mathbf{D}_i$ mentioned in (4). In this study we use the Cholesky decomposition [2] which is a special case of this reparameterisation, i.e. $\mathbf{Q}_i = \text{chol}(\mathbf{D}_i) = \mathbf{L}_i$ where $\mathbf{L}_i$ is lower triangular with positive diagonal entries provided $\mathbf{D}$ is strictly positive definite. Note that d_S is not dependent on using Cholesky versus another decomposition since any two decomposition matrices of the same tensor are related via an orthogonal transformation.

We propose Algorithm 1 for computation of the weighted Procrustes mean.

Algorithm 1 Computation of Weighted Procrustes Mean

Initial setting: $\mathbf{Q}_i^P \leftarrow \text{chol}(\mathbf{D}_i)$, $i = 1, ..., N$
S_W from previous iteration: $S_p \leftarrow 0$
S_W from current iteration:
$S_c \leftarrow \sum_{i=1}^{N} w_i \parallel \mathbf{Q}_i^P - \sum_{j=1}^{N} w_j \mathbf{Q}_j^P \parallel^2$
while $|S_p - S_c| >$ tolerance **do**
  for $i = 1$ to N **do**
    $\hat{\mathbf{Q}}_i = \frac{1}{1-w_i} \sum_{j \neq i} w_j \mathbf{Q}_j^P$
    Calculate the $\hat{\mathbf{R}}_i$ minimising $\parallel \hat{\mathbf{Q}}_i - \mathbf{Q}_i^P \mathbf{R}_i \parallel$ (Procrustes size-and-shape metric)
    $\mathbf{Q}_i^P \leftarrow \mathbf{Q}_i^P \hat{\mathbf{R}}_i$
  end for
  $S_p \leftarrow S_c$
  $S_c \leftarrow \sum_{i=1}^{N} w_i \parallel \mathbf{Q}_i^P - \sum_{j=1}^{N} w_j \mathbf{Q}_j^P \parallel^2$
end while
$\hat{\mathbf{Q}}_W \leftarrow \sum_{i=1}^{N} w_i \mathbf{Q}_i^P$
return $\hat{\mathbf{Q}}_W$

The weighted Procrustes averaging can be applied to diffusion tensor smoothing and interpolation problems. Some experimental results can be seen in Section V.

C. Choice of weights

For any application we have some choice of weights w_i where $w_i \geq 0$ and $\sum_{i=1}^{N} w_i = 1$. For example, w_i could be a decreasing function of the Euclidean distance from the location of interest to the sampling locations i. A simple setting for the weights is with the inverse distance function given by

$$w_i = \frac{d_i^{-1}}{\sum_{j=1}^{N} d_j^{-1}}, i = 1, ..., N \qquad (16)$$

where d_i is the Euclidean distance from the location (voxel) at which the weighted mean is to be estimated, to the location (voxel) of ith tensor $\mathbf{D}_i$.

For more flexibility of weights, an exponential weight function is proposed and used in this paper as follows:

$$w_i = \frac{\exp(-Ad_i^2) + B}{\sum_{j=1}^{N} [\exp(-Ad_j^2) + B]}, i = 1, ..., N \quad (17)$$

where $A, B \geq 0$. It is clear that the two parameter exponential weight family is very flexible. In this study, we use the exponential weight function. In a region of homogeneous diffusion behaviour, a set of equal weights is preferable. However, for a region with complex diffusion behaviour, the choice of the weight function is application dependent.

IV. Weighted Procrustes Regularisation

In the following, we develop a weighted regularistation model which incorporates the smoothness of local diffusion and regularisation of a prescribed diffusion behaviour. Specifically, the Procrustes size-and-shape metric is adapted in the regularisation model.

A. Weighted regularisation model

Consider a sample of diffusion tensors $\mathbf{D}_1, \ldots, \mathbf{D}_N$ from a noisy tensor field containing N voxels with coordinates $x_i \in \mathbb{Z}^3$ where $i = 1, \ldots, N$. Now we wish to carry out regularisation for the tensor field. We propose a weighted regularisation model which is defined by minimising the following function, with respect to $\Sigma_j \in \Omega_+(3)$, $j = 1, \ldots, N$,

$$\begin{aligned} f &= \sum_{j=1}^{N}\sum_{i=1}^{N} w_{ij} d_1^p(\mathbf{D}_i, \Sigma_j) + \lambda \sum_{j=1}^{N} d_2^q(\Pi, \Sigma_j) \\ &= \sum_{j=1}^{N} \left[\sum_{i=1}^{N} w_{ij} d_1^p(\mathbf{D}_i, \Sigma_j) + \lambda d_2^q(\Pi, \Sigma_j) \right], \quad (18) \end{aligned}$$

where the weights w_{ij} can be obtained via some decreasing function of the Euclidean distance between x_i and x_j, p, $q \geq 0$, and $\lambda > 0$ is a regularisation parameter and Π is a reference tensor, representing the prescribed diffusion behaviour. Note that d_1 and d_2 are general, i.e. can be non-Euclidean and need not be the same. Therefor, the weighted regularisation model (18) is very flexible in the ways in which it deals with smoothness and regularisation.

It is clear that the solution $\hat{\Sigma}_j$, $j = 1, 2, \ldots, N$ to the weighted regularisation model (18) must minimise

$$\sum_{i=1}^{N} w_{ij} d_1^p(\mathbf{D}_i, \Sigma) + \lambda d_2^q(\Pi, \Sigma). \quad (19)$$

Therefore, the procedure to solve (18) is that we solve $\hat{\Sigma}_j$ for each $j = 1, \ldots, N$ individually as follows

$$\hat{\Sigma}_j = \arg \inf_{\Sigma \in \Omega_+(3)} \sum_{i=1}^{N} w_i d_1^p(\mathbf{D}_i, \Sigma) + \lambda' d_2^q(\Pi, \Sigma) \quad (20)$$

where $w_i = w_{ij}/(w_{1j} + w_{2j} + \cdots + w_{Nj} + \lambda)$ and $\lambda' = \lambda/(w_{1j} + w_{2j} + \cdots + w_{Nj} + \lambda)$.

Consider first the case where $d_1 = d_2$ is a Euclidean-based metric $d_{E-based}$ given by

$$d_{E-based} = \| g(\mathbf{D}_1) - g(\mathbf{D}_2) \|, \quad (21)$$

where g is a mapping from $\Omega_+(3)$ to $\Omega(3)$. Note that g is assumed to be defined via the spectral decomposition $\mathbf{D} = \mathbf{V}\Lambda\mathbf{V}^T$, i.e. $g(\mathbf{D}) = \mathbf{V}g(\Lambda)\mathbf{V}^T$, where $g(\Lambda)$ is the diagonal matrix with the $g(\lambda_i)$, $i = 1, 2, 3$ on the main diagonal, and λ_i's are the eigenvalues of $\mathbf{D}$. Assume also that g has an inverse g^{-1}. We list some possible choices of $d_{E-based}$ in Table I. Recall that the Euclidean, root Euclidean, and the log-Euclidean metrics are three special cases of the power Euclidean metric.

TABLE I
Choices of Euclidean-based Metrics

$g(\mathbf{D})$	Metric
$\log(\mathbf{D})$	log-Euclidean
$\mathrm{chol}(\mathbf{D})$	Cholesky
$\mathbf{D}$	Euclidean
$2\mathbf{D}^{1/2}$	Root Euclidean
$\frac{1}{\alpha}\mathbf{D}^{\alpha}$, $\alpha \neq 0$ and $\alpha \in \mathbb{R}$	Power Euclidean

If $p = q = 2$, $d_1 = d_2 = d_{E-based}$ in the weighted regularisation model (18), then there is a unique solution to the model (18) which is given by

$$\widehat{\Sigma}_j = g^{-1}(\widehat{\Delta}_j) \quad (22)$$

where

$$\widehat{\Delta}_j = \frac{\sum_{i=1}^{N} w_{ij} g(\mathbf{D}_i) + \lambda\Pi}{\sum_{i=1}^{N} w_{ij} + \lambda}. \quad (23)$$

For example, if $g(\mathbf{D}) = \frac{1}{\alpha}\mathbf{D}^{\alpha}$, then

$$\widehat{\Sigma}_j = \alpha\widehat{\Delta}_j^{1/\alpha}. \quad (24)$$

If $g(\mathbf{D}) = \log(\mathbf{D})$, then

$$\widehat{\Sigma}_j = \exp\{\widehat{\Delta}_j\}. \quad (25)$$

It is clear that using identical Euclidean-based metrics for the weighted regularisation is straightforward in DTI studies. It is more interesting to compare weighted regularisation methods based on different metrics.

Note $p = 2$ and $q = 0$ gives the weighted Fréchet mean, if $q = 0$ we have a type of M-estimator [26], [22], if $p = 1$ and $q = 0$ we have the geometric median [27], if $p = 2$ and $q = 2$ non-Euclidean type of ridge-regression, and if $p = 2$ and $q = 1$ a non-Euclidean type of LASSO [28].

B. Weighted Procrustes regularisation

Now consider the special case that $(p, q) = (2, 2)$ and $d_1 = d_2 = d_S$ where d_S is the Procrustes size-and-shape metric (see (5)). Then, the weighted Procrustes regularisation model is given by

$$f_{WPS} = \sum_{j=1}^{N}\sum_{i=1}^{N} w_{ij} d_S^2(\mathbf{D}_i, \Sigma_j) + \lambda \sum_{j=1}^{N} d_S^2(\Pi, \Sigma_j). \quad (26)$$

Using the procedure proposed in (20), the solution $\hat{\Sigma}_j$, $j = 1, 2, \ldots, N$ is given by

$$\widehat{\Sigma}_j = \arg \inf_{\Sigma \in \Omega_+(3)} \sum_{i=1}^{N} w_i d_S^2(\mathbf{D}_i, \Sigma_j) + \lambda' d_S^2(\Pi, \Sigma_j). \quad (27)$$

To solve (27) is equivalent to solve

$$\widehat{\Sigma}_j = \arg \inf_{\Sigma \in \Omega_+(3)} \sum_{i=1}^{N+1} w_i d_S^2(\mathbf{D}_i, \Sigma), \quad (28)$$

where $\mathbf{D}_{N+1} = \Pi$ and $w_{N+1} = \lambda'$. Furthermore, the weighted Procrustes averaging (13) in Section III-B is proposed to solve for $(\Sigma_1, \ldots, \Sigma_N)$ which can be computed using Algorithm (1).

The weighted Procrustes regularisation model (26) can be used for tensor field smoothing and interpolation. More importantly, we propose to use the same weighted Procrustes method for segmentation. In this work, we illustrate the approach by simply examples where a single structure of interest can be highlighted and ultimately segmented from a region of interest (ROI). Initial results of the segmentation will be discussed in Section V-E2.

V. Results

Our methods are illustrated on both synthetic and real diffusion tensor data. First, we present a study for comparing the anisotropy measures PA and FA. We then compare different choices of metrics (the Euclidean, log-Euclidean, Riemannian, Cholesky, root Euclidean and Procrustes size-and-shape metrics) using geodesic interpolation and the weighted Procrustes regularisation model is then applied to synthetic data. The weighted Procrustes methods are also applied to smooth and interpolate a tensor field from a healthy human brain. Finally, the initial results of the Procrustes segmentation are reported.

A. Materials

A set of diffusion weighted MR images acquired with the Uniform 32 DTI diffusion gradient direction scheme [29] from a healthy human brain has been used for this study. The MR images were acquired using a spin echo EPI (echo planar imaging) sequence with diffusion weighting gradients applied with a weighting factor of b=1000 s/mm^2 in a Philips 3T Achieva clinical imaging system (Philips Medical Systems, Best, The Netherlands). Throughout the subject's head, 52 interleaved contiguous transaxial slices were acquired in a matrix of 112x112 (interpolated to 224x224) with an acquisition voxel size of 1x1x2 mm^3. For each slice, the acquisition was repeated for each of the 32 non-collinear directions according to the Uniform 32 direction scheme, and once with no diffusion weighting ($b = 0$). A Bayesian estimation method [5] has been employed to compute the tensor field and all methods of this paper are programmed with MATLAB (The Mathworks, Inc., R2008a).

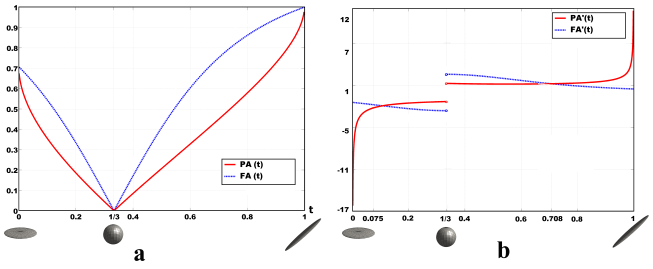

Fig. 1. Comparison of FA and PA. a: Graph of FA and PA values as functions of t. b: Derivatives of FA and PA with respect to t. The x-axis is $t \in [0, 1]$ which defines three eigenvalues as t, $(1-t)/2$ and $(1-t)/2$.

B. Anisotropy study

To compare PA with FA, we first define three eigenvalues of the diffusion tensor as functions of a single parameter t, $0 \leq t \leq 1$, namely $t, (1-t)/2$ and $(1-t)/2$ (e.g. [8]). Figure 1a shows a comparison of the FA and PA values as t increases from 0 to 1. The diffusion tensor varies from planar to spherical as t increases from 0 to 1/3. The tensor then becomes linear as t grows to 1. Recall that the PA value is always dominated by the corresponding FA value (see APPENDIX). Figure 1b shows the first derivative of FA and PA with respect to t. Approximately when $t < 0.075$ or $t > 0.708$, $|\mathrm{PA}'(t)|$ is larger than $|\mathrm{FA}'(t)|$. This means PA is more sensitive to changes in highly planar or highly linear anisotropy of diffusion than FA.

Now let us compare FA and PA maps from real data. Figure 2a and 2b are FA and PA maps (axial slices) computed from the healthy human brain data. The splenium in the corpus callosum is one of the regions where the overall anisotropy is very high [30]. We take the FA and PA values along the green line in the splenium and show them in Figure 2c in detail. PA has notably higher variation than FA. In summary, PA offers better contrast in highly anisotropic regions.

C. Geodesic interpolation

Now we carry out three experiments to investigate the geometric nature of geodesic paths obtained with the different metrics d. Specifically, we choose two tensors of interest as the end "points" of a geodesic, and then interpolate between them by sampling seven additional tensors along the geodesic as follows:

$$\mathbf{D}_i = \arg \inf_{\mathbf{D}} \frac{(9-i)}{8} d^2(\mathbf{D}_1, \mathbf{D}) + \frac{(i-1)}{8} d^2(\mathbf{D}_9, \mathbf{D}), \quad (29)$$

where $1 < i < 9$, $\mathbf{D}_1$ and $\mathbf{D}_9$ are the original tensors. For each tensor $\mathbf{D}$ on the geodesic, we measure its size (volume) of $\mathbf{D}$ by $|\mathbf{D}|$, the determinant, and the anisotropy by PA($\mathbf{D}$) and FA($\mathbf{D}$). We also measure orientation of $\mathbf{D}$ by ϕ defined in (30) as the angle between the principal directions (eigenvectors) of $\mathbf{D}$ and $\mathbf{D}_1$.

$$\phi = \arcsin(\| \mathbf{pv}_1 \times \mathbf{pv}_i \|), i = 1, ..., 9 \quad (30)$$

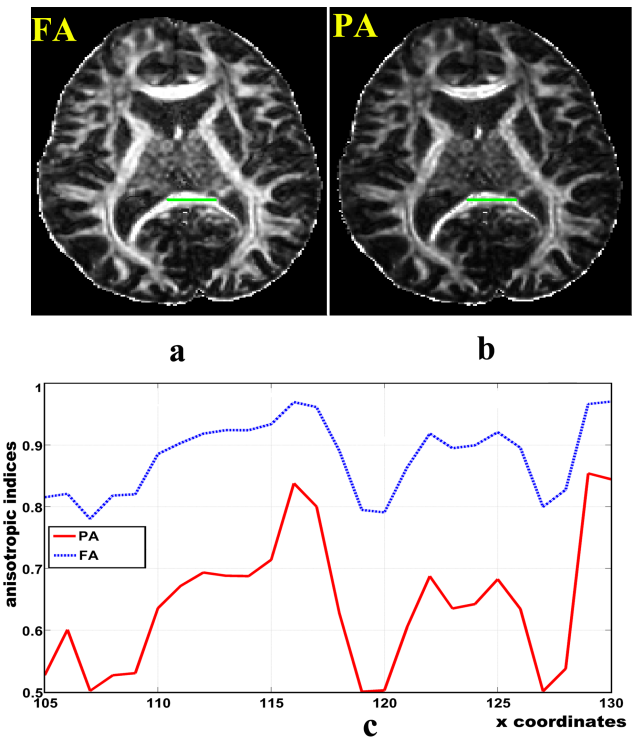

Fig. 2. Comparison of FA and PA in the splenium. Anisotropy maps from axial view. a: FA map. b: PA map. c: Graph of FA and PA values along the green line in a and b.

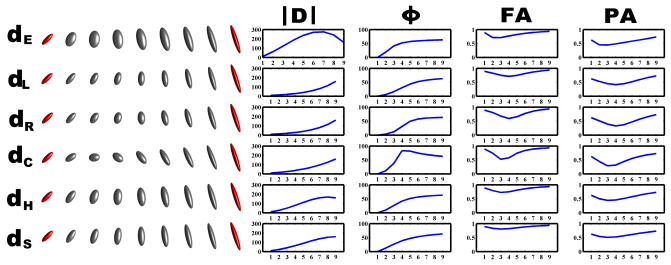

Fig. 3. Geodesic paths between two general tensors. Two tensors $\mathbf{D}_1$ (left in red) and $\mathbf{D}_9$ (right in red) with general (i.e. non-collinear, non-orthogonal) orientation, different shape and size. The geodesic paths are obtained with d_E, d_L, d_R, d_C, d_H and d_S.

where $\mathbf{pv}_i$ is the principal eigenvector of $\mathbf{D}_i$. First, we focus on the evolution of the size, shape and orientation through the geodesic paths. The setting of $\mathbf{D}_1$ and $\mathbf{D}_9$ is general, specifically the two tensors are $\phi = 63°$ apart, have (10,1,1) and (40,4,1) as their respective spectra, and therefore differ in shape and size. Six metrics are considered, namely the Euclidean (d_E), log-Euclidean (d_L), Riemannian (d_R), Cholesky (d_C), root Euclidean (d_H) and Procrustes size-and-shape (d_S). Figure 3 shows samples from the six geodesic paths. This example confirms that the Euclidean metric is very problematic, especially due to the parabolic interpolation of the determinant. The Procrustes metric offers somewhat better interpolation in terms of orientation and anisotropy (see graphs of ϕ, FA and PA). The Cholesky path has a significant cusp in

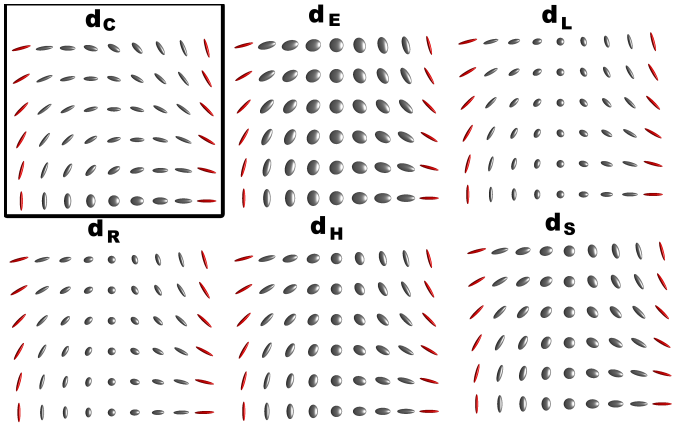

Fig. 4. Geodesic paths under simultaneous rotation of two tensors (red) with different metrics.

the tensor's volume, orientation and anisotropy in this example. In general, the log-Euclidean, Riemannian and Procrustes size-and-shape methods seem preferable.

Another experiment is carried out to illustrate the geometry of geodesic path under rotation. Specifically, it is known [19] that all of the metrics considered here, except d_C, are invariant to orthogonal transformations of the underlying 3D space, i.e. $d(\mathbf{U}\mathbf{D}_1\mathbf{U}^T, \mathbf{U}\mathbf{D}_2\mathbf{U}^T) = d(\mathbf{D}_1, \mathbf{D}_2)$ where $\mathbf{U} \in O(3)$. This is very important in practice as any method for diffusion tensor processing must be independent of the choice of the reference frame. Here, we emphasize that all of the considered linear interpolations using d_S and the Euclidean-based metrics, apart from the Cholesky-based one, are invariant to the orthogonal transformations, and therefore are indeed independent of the choice of the reference frame. The d_R-based geodesics are also independent of the choice of the reference frame. The experiment is described as follows:

1. Obtain six pairs of diffusion tensors by simultaneous rotation.
   - 1.1 Start with two orthogonal tensors $\mathbf{D_1}$ and $\mathbf{D_9}$ with the same setting of eigenvalues (40, 2, 1). Since the largest eigenvalue is much greater than the other two eigenvalues, $\mathbf{D_1}$ and $\mathbf{D_9}$ are nearly linear and their principal eigenvectors are orthogonal.
   - 1.2 Rotate the eigenstructures of $\mathbf{D_1}$ and $\mathbf{D_9}$ simultaneously along the z-axis with step size of 15°.
2. Plot the geodesic paths of each pair of tensors with different metrics.

Figure 4 shows the geodesic paths of each pair of synthetic tensors (red) with different metrics respectively. It is clear that the geodesic path obtained with the Cholesky approach is not invariant under the simultaneous rotation of $\mathbf{D_1}$ and $\mathbf{D_9}$, although all the other paths are.

Figure 5 shows interpolations of the four synthetic tensors at the corners of a grid using the Euclidean, Pro-

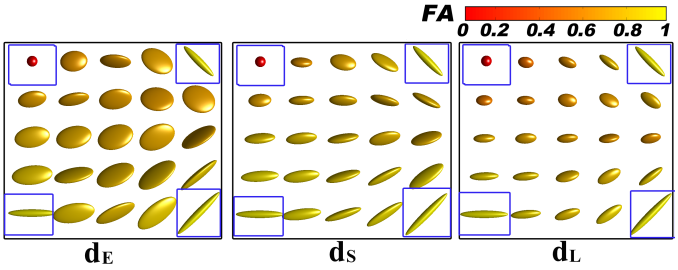

Fig. 5. Interpolation of four tensors at the corners of a grid with FA colouring. Left: Euclidean interpolation (d_E). Middle: Procrustes interpolation (d_S). Right: log-Euclidean interpolation (d_L). FA is used for colouring the tensors.

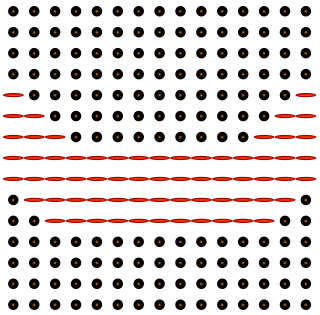

Fig. 6. A synthetic diffusion tensor field with a U-shaped bundle of anisotropic tensors in an isotropic environment.

crustes and log-Euclidean metrics. Again, the swelling effect appears in the Euclidean case. The log-Euclidean interpolation tends to produce smaller tensors. It may be argued that the Procrustes metric provides a reasonable interpolation of the tensor size. Indeed, the tensors near the top right corner are reasonably small, and the size increases smoothly as we approach the bottom right corner. We colour the tensors with their FA values. Graphs of FA and PA in Figure 5 suggests that the Procrustes method may also be preferable as far as FA and PA interpolation is concerned.

D. Weighted Procrustes Regularisation of synthetic data

A synthetic diffusion tensor field was generated by placing a U-shaped bundle of anisotropic tensors in an isotropic environment (see Figure 6). Tensors in the anisotropic bundle have eigenvalues $\lambda_1 = 1000$, $\lambda_2 = \lambda_3 = 200$ and horizontal orientation (i.e. the principal eigenvector is [1,0,0]). The isotropic tensors have the following eigenvalues $\lambda_1 = \lambda_2 = \lambda_3 = 500$. We generate a noisy tensor $\mathbf{D}^*$ from each noise-free tensor $\mathbf{D}$ in the tensor field as follows

1 Obtain $\mathbf{D}^{1/2} = \begin{pmatrix} \sqrt{\lambda_1} & 0 & 0 \\ 0 & \sqrt{\lambda_2} & 0 \\ 0 & 0 & \sqrt{\lambda_3} \end{pmatrix}$ (since all the original tesnors are diagonal in the canonical basis (1,0,0), (0,1,0),(0,0,1)).

2 Let Δ be a 3×3 matrix. Then sample $vec(\Delta) \sim N(vec(\mathbf{D}^{1/2}), \sigma^2 \mathbf{I}_9)$ where the operator vec vectorises a matrix by stacking all columns, $\mathbf{I}_9$ is the 9×9 identity matrix, and N stands for 'multivariate normal distribution'.

3 The noisy synthetic diffusion tensor is $\mathbf{D}^* = \Delta\Delta^T$.

We do a series of controlled simulations, using an error measure to choose an optimal value for the regularisation parameter λ. The error measure e_{FA} is defined in (31) below and measures discrepancy between the regularised field and the original, noise-free field.

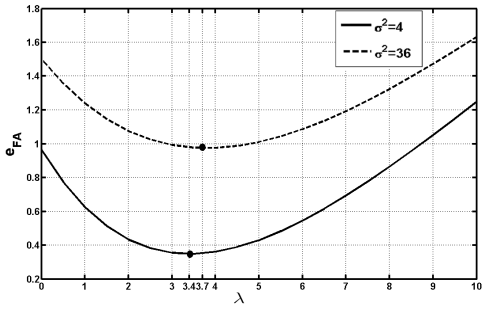

Fig. 7. Regularisation error e_{FA} as a function of the regularisation parameter λ, and the variance of noise $\sigma^2 = 4$ and 36.

$$e_{FA} = \sum_{i=1}^{N} \mathrm{FA}_i (\mathrm{FA}_i - \hat{\mathrm{FA}}_i)^2 \tag{31}$$

where N is the total number of diffusion tensors in the field, FA_i is the true FA value of the ith original tensor and $\hat{\mathrm{FA}}_i$ is the FA value of the corresponding regularised tensor. The measure e_{FA} upweights the errors from the anisotropic part of the field, which is of more interest to us. Figure 7 shows the error measure e_{FA} as a function of the regularisation parameter λ, and for two levels of noise $\sigma^2 = 4$ and 36. We define the reference tensor $\Pi = [5,0,0;0,1,0;0,0,1]$. Two parameters A and B in (17) for setting the weights are 2 and 0.01. The optimal values of λ for $\sigma^2 = 4$ and 36 are 3.4 and 3.7 respectively. Table II additionally shows optimal λ values for several other levels of noise. Experimentally, we notice that as the noise level σ^2 decreases, the optimal regularisation parameter λ decreases to about 3.

TABLE II
OPTIMAL VALUES OF THE REGULARISATION PARAMETER λ FOR DIFFERENT LEVELS OF NOISE.

σ^2	100	25	10	1	0.01	0.001
optimal λ	8.100	5.500	3.330	3.260	3.130	3.124

Figure 8 shows results of the regularisations of two synthetic fields corrupted with noise of level $\sigma^2 = 4$ and 36. The regularised images are much smoother than the noisy images. In particular, the smoothness of the anisotropic part for $\sigma^2 = 36$ is largely improved in the regularised image.

E. Real data

1) Weighted Procrustes for Smoothing and interpolation: Using the weighted Procrustes analysis (see Section

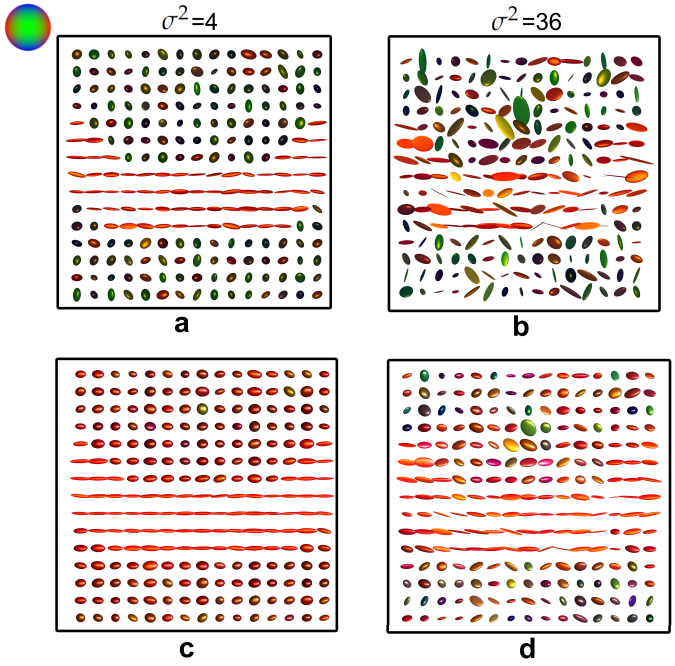

Fig. 8. Synthetic (a,b) and regularised (c,d) tensor fields with noise variance $\sigma^2 = 4$ (a,c) and $\sigma^2 = 36$ (b,d). Color-coding is by principal diffusion direction with red, green and blue representing diffusion in the x, y and z axes respectively.

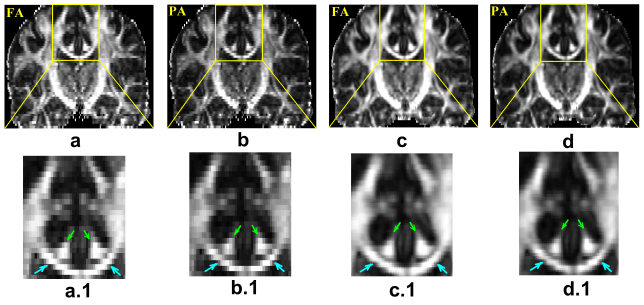

Fig. 9. Smoothing and interpolation of the human brain diffusion tensor data. FA (a) and PA (b) maps based on tensor estimates without post-processing. FA (c) and PA (d) maps from smoothed and interpolated tensor data obtained with the weighted Procrustes averaging method. (a.1), (b.1), (c.1) and (d.1) are zoomed inset regions in the yellow box.

III-B), we smooth and interpolate (with two equally spaced interpolation points between each pair of original voxels) the diffusion tensor data from the human brain, and calculate the FA and PA maps shown in Figure 9. Two parameters A and B in (17) for setting the weights are 2 and 0.01. It is clear that the FA and PA maps from the processed tensor data are much smoother than the ones without the processing. The feature that the cingulum (cg) is distinct from the corpus callosum (cc) is clearer in the anisotropy maps from the processed data than in those without the processing [19].

2) Weighted Procrustes for Segmentation: The weighted Procrustes regularisation method is applied to segment structures of interest from the real DTI data. Figure 10 shows the initial results of the corpus callosum with

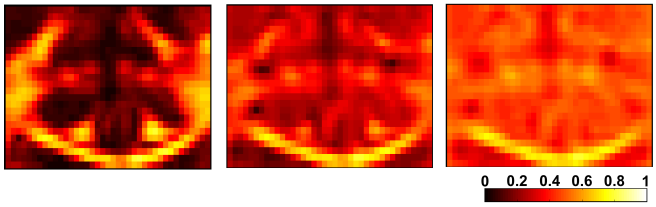

Fig. 10. Segmentation of the corpus callosum (FA map) with the reference tensor [0.0022,0,0; 0, 0.0004,0; 0,0, 0.0004]. Left: the regularisation parameter $\lambda = 0.1$. Middle: $\lambda = 0.6$. Right: $\lambda = 1.5$.

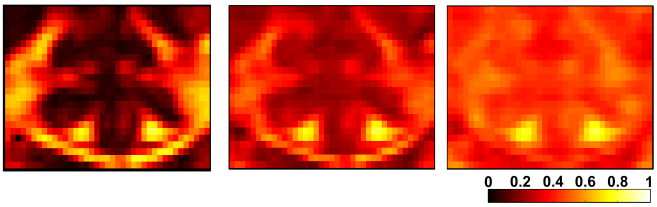

Fig. 11. Segmentation of the cingulum (FA map) with the reference tensor [0.0003,0,0;0,0.0015,0;0,0,0.0002]. Left: the regularisation parameter $\lambda = 0.1$. Middle: $\lambda = 0.6$. Right: $\lambda = 1.5$.

regularisation parameter $\lambda = 0.1$, 0.6 and 1.5. The reference tensor is [0.0022,0,0; 0, 0.0004,0; 0,0, 0.0004][1] which is highly anisotropic and the diffusion direction is parallel to the x axis. Two parameters A and B in (17) for setting the weights are 2 and 0.01. It is clear that as λ increases the FA map becomes blurred except in the corpus callosum. Figure 11 shows the results of the cingulum segmentation with the reference tensor [0.0003,0,0;0,0.0015,0;0,0,0.0002]. When $\lambda = 1.5$, the cingulum can be easily segmented from the image (using, for example, a simple thresholding).

VI. Discussion

We presented a weighted Procrustes averaging method for defining the mean tensor in a diffusion tensor image. A weighted regularisation model using the Procrustes size-and shape metric has also been proposed for tensor field regularisation. The proposed regularisation simultaneously smooths each tensor **D** based on the information provided by the tensor's neighbours (endogenous regularisation) and also makes **D** mimic a reference tensor (exogenous regularisation) according to suitable tensor metrics. The flexibility of having a reference tensor can be exploited to introduce additional information about the expected diffusion profile in the given region, or to highlight, and eventually segment, local structures.

We applied our methods and models to smooth and interpolate the entire tensor field within a region as well as to segment a structure of particular interest. The weighted regularisation framework proposed in Section IV is very general. Presently, we have considered the special case with the power parameters $p = q = 2$

[1]The reference tensor is already on the real scale that is determined by the b-value of 1000 s/mm^2

and the Procrustes size-and-shape metric being used for both d_1 (endogenous regularisation) and d_2 (exogenous regularisation). It would be interesting to vary the parameters in the weighted regularisation model. For example, when $p = 2$ and $q = 2$, we have a generalised (non-Euclidean) type of ridge-regression model. When $p = 2$ and $q = 1$, the method gives a generalised (non-Euclidean) type of LASSO [28], and so on. To develop an efficient and more automated method for choosing the regularisation parameter λ is also one of the aims for our future work.

There is a challenge to process tensor fields containing multiple diffusion profiles, especially when more than one distinct profile is observed at a single voxel (crossing fibres, etc). For example, to interpolate a pair of tensors at one voxel with a pair of tensors at another voxel is a basic problem. An intuitive idea is to find the optimal matches between two pairs, i.e. to match each tensor at the first voxel with a tensor at the second voxel. Then, the processing can be carried out between matched tensors. Also, when more angular directions are available such as in HARDI data [32] more flexible models than diffusion tensors can be explored, which presents more challenges for non-Euclidean statistical analysis.

APPENDIX

Lemma For any non-zero symmetric semi-positive definite $\mathbf{D}$, $\mathrm{FA}(\mathbf{D}^\alpha)$ is an increasing function of $\alpha \in (0, \infty)$.

Proof: Let $a, b > 0$ be such that $a \leq b$. We need to show that

$$\frac{\sum_{i=1}^{3}(\lambda_i^a - \overline{\lambda^a})^2}{\sum_{i=1}^{3}\lambda_i^{2a}} \leq \frac{\sum_{i=1}^{3}(\lambda_i^b - \overline{\lambda^b})^2}{\sum_{i=1}^{3}\lambda_i^{2b}}. \tag{A-1}$$

Equivalently, we need to show

$$[\overline{\lambda^b}]^2\overline{\lambda^{2a}} \leq [\overline{\lambda^a}]^2\overline{\lambda^{2b}}. \tag{A-2}$$

Let $q = \frac{2b-a}{b}$, $p = \frac{2b-a}{b-a}$, so that $\frac{1}{q} + \frac{1}{p} = 1$, $p \geq 1, q \geq 1$, then write $\lambda_i^b = \lambda_i^{s+t}$, $i \in \{1,2,3\}$ where $s = \frac{a}{q} = \frac{ab}{2b-a}$, $t = \frac{2b}{p} = \frac{2b(b-a)}{2b-a}$.

Apply Hölder's inequality [31] with $g_i = \lambda_i^s$, $f_i = \lambda_i^t$,$i \in 1,2,3$,

$$\sum_{i=1}^{3}|g_i f_i| \leq [\sum_{i=1}^{3} g_i^q]^{1/q}[\sum_{i=1}^{3} f_i^p]^{1/p} \tag{A-3}$$

to obtain

$$\begin{aligned} &\overline{\lambda^b} \leq [\overline{\lambda^a}]^{\frac{b}{2b-a}}[\overline{\lambda^{2b}}]^{\frac{b-a}{2b-a}} \\ \Longrightarrow\ &[\overline{\lambda^b}]^2 \leq [\overline{\lambda^a}]^{\frac{2b}{2b-a}}[\overline{\lambda^{2b}}]^{\frac{2b-2a}{2b-a}}. \end{aligned} \tag{A-4}$$

Next, take $q' = \frac{2b-a}{2b-2a}$, $p' = \frac{2b-a}{a}$, note that $p', q' \geq 1$, $\frac{1}{q'} + \frac{1}{p'} = 1$. Then write $\lambda_i^{2a} = \lambda_i^{s'+t'}$, and take $s' = \frac{a}{q'} = \frac{2a(b-a)}{2b-a}$, $t' = \frac{2b}{p'} = \frac{2ab}{2b-a}$. Again, let $g_i' = \lambda_i^{s'}$, $f_i' = \lambda_i^{t'}$, $i \in \{1,2,3\}$ and apply Hölder's inequality to get

$$\overline{\lambda^{2a}} = \overline{\lambda^{s'+t'}} \leq [\overline{\lambda^a}]^{\frac{2(b-a)}{2b-a}}[\overline{\lambda^{2b}}]^{\frac{a}{2b-a}}. \tag{A-5}$$

Finally, multiply both sides of inequality (A-4) by respective sides of inequality (A-5) to obtain inequality (A-2). ■

ACKNOWLEDGMENT

This work was supported by the European Commission FP6 Marie Curie Action Programme under the CMIAG (Collaborative Medical Image Analysis on Grid) project. The diffusion MR image data used in this paper is provided by the Division of Academic Radiology, University of Nottingham and Queen's Medical Centre, UK, and the authors would like to thank Dr Paul Morgan and Professor Dorothee Auer for their assistance.

REFERENCES

[1] Alexander, D. C. (2005). Multiple-fibre reconstruction algorithms for diffusion MRI. *Annals of the New York Academy of Sciences*, 1046:113–133.

[2] Koay, C. G., Carew, J. D., Alexander, A. L., Basser, P. J., and Meyerand, M. E. (2006). Investigation of anomalous estimates of tensor-derived quantities in diffusion tensor imaging. *Magnetic Resonance in Medicine*, 55:930–936.

[3] Kingsley, P. B. (2006). Introduction to diffusion tensor imaging mathematics: Part III. tensor calculation, noise, simulations, and optimisation. *Concepts in Magnetic Resonance Part A*, 28A:155–179.

[4] Behrens, T. E, Woolrich, M. W, Jenkinson, M., Johansen-Berg, H., Nunes, R. G., Clare, S., Matthews, P. M., Brady, J. M., and Smith, S. M. (2003). Characterisation and propagation of uncertainty in diffusion-weighted MR imaging. *Magnetic Resonance in Medicine*, 50:1077–1088.

[5] Zhou, D., Dryden, I. L., Koloydenko, A. A, and Bai, L. (2008). A Bayesian method with reparameterisationfor diffusion tensor imaging. In *Proceedings of SPIE Medical Imaging 2008: Image Processing, 69142J. Edited by J. M. Reinhardt and J. P. W. Pluim.*

[6] Basser, P. J., Mattiello, J., and Le Bihan, D. (1994). Estimation of the effective self-diffusion tensor from the NMR spin echo. *Journal of Magnetic Resonance. Series B*, 103:247–254.

[7] Wheeler-Kingshott, C. A., Barker, G. J., Steens, S. C., and Buchem, M. A. v. (2003). *Quantitative MRI of the Brain: measuring changes caused by disease*, chapter 7: the Diffusion of Water, pages 203–256. John Wiley & Sons Ltd.

[8] Batchelor, P. G., Moakher, M., Atkinson, D., Calamante, F., and Connelly, A. (2004). A rigorous framework for diffusion tensor calculus. *Magnetic Resonance in Medicine*, 53(1):221–225.

[9] Le Bihan, D., Mangin, J. F., Poupon, C., Clark, C. A., Pappata, S., Molko, N., and Chabriat, H. (2001). Diffusion tensor imaging: concepts and applications. *Journal of Magnetic Resonance Imaging*, 13:534–546.

[10] Basser, P. J., Pajevic, S., Pierpaoli, C., Duda, J., and Aldroubi, A. (2000). In vivo fibre tractography using DT-MRI data. *Magnetic Resonance in Medicine*, 44:625–632.

[11] Le Bihan, D., Poupon, C., Amadon, A., and Lethimonnier, F. (2006). Artifacts and pitfalls in diffusion MRI. *Journal of Magnetic Resonance Imaging*, 24:478–488.

[12] Coulon, O., Alexander D. C., and Arridge S. (2004). Diffusion tensor magnetic resonance image regularization. *Medical Image Analysis*, 8:47–67.

[13] Wiegell, M.R., Tuch, D.S., Larson, H.W.B., and Wedeen, V.J. (2003). Automatic segmentation of thalamic nuclei from diffusion tensor magnetic resonance imaging. *NeuroImage*, 19:391–402.

[14] Zhukov, L., Museth, K., Breen, D., Whitaker, R., and Barr, A. H. (2003). Level set segmentation and modeling of DT-MRI human brain data. *Journal of Electronic Imaging*, 12:125–133.

[15] Wang, Z. and Vemuri, B. C. (2004). Tensor field segmentation using region based active contour model. *Proc ECCV*, 304–315.

[16] Arsigny, V., Fillard, P., Pennec, X., and Ayache, N. (2006). Log-Euclidean metrics for fast and simple calculus on diffusion tensors. *Magnetic Resonance in Medicine*, 56:411–421.
[17] Pennec, X., Fillard, P., and Ayache, N. (2006). A Riemannian framework for tensor computing. *International Journal of Computer Vision*, 66:41–66.
[18] Fletcher, P. T. and Joshi, S. (2007). Riemannian geometry for the statistical analysis of diffusion tensor data. *Signal Process*, 87(2):250–262.
[19] Dryden, L. I., Koloydenko, A. A., and Zhou, D. (2009). Non-Euclidean statistics for covariance matrices, with applications to diffusion tensor imaging. *Annals of Applied Statistics*, 3:1102–1123.
[20] Zhou, D., Dryden, I. L., Koloydenko, A. A, and Bai, L. (2009). Procrustes analysis of diffusion tensor data In *Proceedings 17th Scientific Meeting, International Society for Magnetic Resonance in Medicine*, Honolulu, page 3584.
[21] Gower, J. C. (1975). Generalized Procrustes analysis. *Psychometrika*, 40:33–50.
[22] Dryden, L. I. and Mardia, K. V. (1998). *Statistical Shape Analysis*. Wiley & Sons, Chichester.
[23] Goodall, C. R.(1991). Procrustes methods in the statistical analysis of shape. *Journal of the Royal Statistical Society. Series B (Methodological)*, 53:285–339.
[24] Kingsley, P. B. (2006). Introduction to diffusion tensor imaging mathematics: Part II. Anisotropy, Diffusion-weighting factors, and gradient encoding schemes. *Concepts in Magnetic Resonance Part A*, 28A:123–154.
[25] Fréchet, M. (1948). Les éléments aléatoires de nature quelconque dans un espace distancié. *Annales de l'institut Henri Poincaré*, 10(4):215–310.
[26] Kent, J. T. (1992). New directions in shape analysis. *In Mardia, K. V., editor, The Art of Statistical Science*, 115-127. Wiley, Chichester.
[27] Fletcher, P. T., Venkatasubramanian, S., and Joshi, S. (2009). The geometric median on Riemannian manifolds with application to robust atlas estimation. *Neuroimage*, 45:S143-S152.
[28] Tibshirani, R. (1996). Regression shrinkage and selection via the lasso. *Journal of the Royal Statistical Society. Series B (Methodological)*, 58:267–288.
[29] Sotiropoulos, S. N., Bai, L, Morgan, P.S., Auer, D.P., Constantinescu, C.S., and Tench, C.R.(2008). A regularized two-tensor model fit to low angular resolution diffusion images using basis directions. *Journal of Magnetic Resonance Imaging* , 28:199-209.
[30] Lee, C. E. C. and Danielian, L. E. and Thomasson, D. and Baker, E. H. (2009). Normal regional fractional anisotropy and apparent diffusion coefficient of the brain measured on a 3T MR scanner. *Neuroradiology*, 51:3–9.
[31] Mirsky, L. (1955). *An introduction to linear algebra*. Clarendon Press, Oxford.
[32] Tuch, D.S., Reese, T.G., Wiegell, M.R., Makris, N., Belliveau, J.W. and Wedeen, V.J. (2002). High angular resolution diffusion imaging reveals intravoxel white matter fiber heterogeneity. *Magnetic Resonance in Medicine*, 48:577–582.